

Enhancing Resonant Second-Harmonic Generation in Bilayer WSe₂ by Layer-Dependent Exciton-Polaron Effect

Soonyoung Cha, Tianyi Ouyang, Takashi Taniguchi, Kenji Watanabe, Nathaniel M. Gabor,* and Chun Hung Lui*



Cite This: *Nano Lett.* 2024, 24, 14847–14853



Read Online

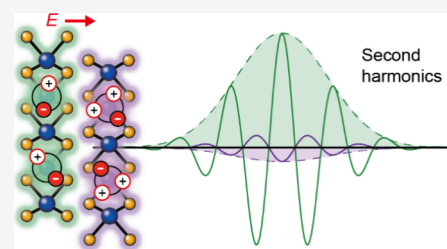
ACCESS |

Metrics & More

Article Recommendations

Supporting Information

ABSTRACT: Two-dimensional (2D) materials serve as exceptional platforms for controlled second-harmonic generation (SHG). Current approaches to SHG control often depend on nonresonant conditions or symmetry breaking via single-gate control. Here, we employ dual-gate bilayer WSe₂ to demonstrate an SHG enhancement concept that leverages strong exciton resonance and a layer-dependent exciton-polaron effect. By selectively localizing injected holes within one layer, we induce exciton-polaron states in the hole-filled layer while maintaining normal exciton states in the charge-neutral layer. The distinct resonant conditions of these layers effectively break interlayer inversion symmetry, thereby promoting resonant SHG. This method achieves a remarkable 40-fold enhancement of SHG at minimal electric field, equivalent to conditions near the dielectric-breakdown threshold but using only ~3% of the critical breakdown field. Our results highlight SHG sensitivity to carrier density and type, offering a new tool for manipulating SHG and probing quantum states in 2D excitonic systems.



KEYWORDS: *Second-harmonic generation, Two-dimensional materials, Exciton, Layered transition metal dichalcogenides, Nonlinear optical phenomena*

Second-harmonic generation (SHG), where two identical photons combine into a single photon with double frequency, plays a pivotal role in various scientific disciplines such as nonlinear frequency conversion, quantum optics, materials characterization, surface studies, and biological imaging.^{1–3} Two-dimensional (2D) crystals, including transition metal dichalcogenides (TMDs) like MoS₂ and WSe₂, stand out as exceptional media for SHG. These materials exhibit selective inversion symmetry based on their layer numbers^{4,5} and stacking arrangements.^{6–9} For instance, monolayer WSe₂, lacking inversion symmetry, exhibits robust SHG.^{10,11} However, stacking two such monolayers with opposite layer orientations results in SHG phases that cancel each other out, leading to no net SHG (Figure 1a).

In addition to varying layer thickness, researchers explore different approaches to control SHG in 2D crystals.^{12–16} Notably, applying an electric field can break the inversion symmetry of bilayers, thereby disrupting destructive SHG interference between layers and promoting emergent SHG (Figure 1b). However, the SHG efficiency remains relatively low due to the weak modulation of quantum states by the electric field. Moreover, increasing the electric field poses risks, such as dielectric breakdown and instabilities in devices. Other methods, such as surface layer attachment¹⁴ and layer-dependent phase transitions,¹⁵ exhibit inconvenience and limited effectiveness.

In this study, we focus on bilayer WSe₂ as a model system to demonstrate an innovative approach to enhance SHG. Our

method leverages the strong exciton resonance and the distinctive layer-dependent exciton-polaron effect in 2D TMD semiconductors. Specifically, we exploit two key features of typical TMD bilayers: (1) their holes are localized within one layer; (2) they host robust intralayer excitons that interact strongly with ambient holes in the same layer to form layer-specific exciton polarons. By applying an electric field to create an interlayer potential difference, we selectively inject holes into one layer while maintaining the other layer as charge-neutral. This approach allows us to create normal exciton states in the charge-neutral layer but exciton-polaron states in the hole-filled layer. Unlike excitons, exciton polarons exhibit lower energy and a much weaker resonant effect with SHG.¹¹ When performing SHG at the exciton energy, the layer with exciton states generates strong resonant second-harmonic waves, while the layer with exciton-polaron states exhibits a minimal response. The lack of destructive interference between them results in a pronounced net SHG signal (Figure 1c).

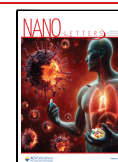
Our approach, founded on the layer-dependent exciton-polaron effect, represents a conceptual departure from previous methods that depend on nonresonant conditions and/or

Received: September 15, 2024

Revised: October 29, 2024

Accepted: November 5, 2024

Published: November 11, 2024



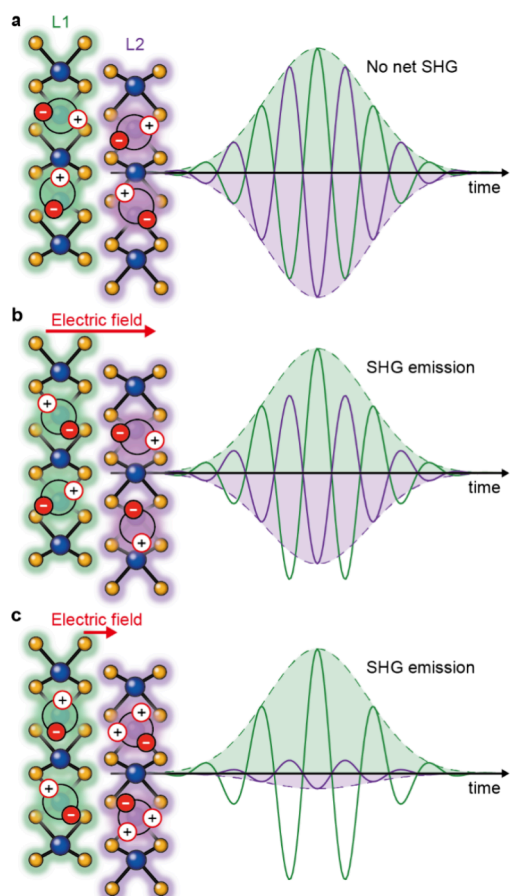


Figure 1. Schematic resonant second-harmonic generation (SHG) from 2H-stacked bilayer WSe_2 . (a) Both WSe_2 layers (L1 and L2) host intralayer exciton states, producing opposite second-harmonic signals that cancel each other out, resulting in zero net SHG. (b) Application of an inversion-symmetry-breaking electric field disrupts the destructive interference, allowing for a finite net SHG signal. (c) By selectively injecting holes into one layer to induce layer-specific exciton-polaron states, while maintaining normal exciton states as the charge-neutral layer, distinct resonant behaviors of the two layers lead to enhanced SHG signals.

symmetry breaking via single-gate control.^{17–19} By independently controlling charge density and electric field in dual-gate devices, our method demonstrates a remarkable 40-fold enhancement of SHG at a minimal electric field. Notably, we achieve SHG emission comparable to that induced near the dielectric-breakdown threshold with just $\sim 3\%$ of the critical breakdown field. The ability to achieve such substantial SHG enhancement at minimal electric fields opens new avenues for experimental setups and applications in which high electric fields are impractical.

We fabricate dual-gated 2H-stacked bilayer WSe_2 encapsulated by hexagonal boron nitride (BN). Thin graphite flakes are used as contacts and gate electrodes to improve the device performance. The dual-gate configuration enables us to independently control the charge density (electric field) by applying voltages of the same sign (opposite signs) to the top and bottom gates. We measure the SHG from bilayer WSe_2 under the excitation of an ultrafast laser with tunable wavelength (PHAROS + ORPHEUS, Light Conversion Inc.). All measurements are conducted at sample temperature $T \approx 6$ K to minimize thermal fluctuation and spectral

broadening of the exciton states. Detailed experimental methods are provided in the [Methods](#) section. The results in the main paper are obtained on Device 1, and additional results on Device 2 are presented in the [Supporting Information](#).

We first compare the influences of the electric field and charge density on the SHG of bilayer WSe_2 ([Figure 2](#)). In the measurement, we set the laser wavelength to 1449 nm, so that the second-harmonic energy (1.712 eV) matches the A exciton resonance in bilayer WSe_2 . The A exciton, consisting of an electron–hole pair in the K valley, is essentially an intralayer state because both the electron and hole wave functions are predominantly localized in the same layer.^{20,21} Indeed, we can consider the bilayer K valleys as two decoupled monolayer valleys in Layers 1 and 2 (denoted as L1 and L2 valleys), whose energies are the same, because the two layers are connected by inversion symmetry. When an electric field is applied to break the inversion symmetry, the degeneracy between the L1 and L2 valleys will be lifted ([Figure 2a](#)).

[Figure 2b,c](#) display the SHG under varying electric fields (E) at zero carrier density (N). In these conditions, both layers are charge-neutral (denoted as the *i-i* regime since both layers are intrinsic). At zero field, the SHG signal is zero as expected because of inversion symmetry. But when the field increases, the SHG emerges due to the breaking of inversion symmetry.¹⁸ The electric field can reach $E \sim 0.15$ V/nm before the device undergoes dielectric breakdown. In comparison, we also measure the bilayer SHG at varying charge densities but zero electric fields ([Figure 2d–f](#)). As inversion symmetry is preserved in this case, the two monolayer valleys remain energy-degenerate. The injected charges are distributed equally between the two layers ([Figure 2d](#)). Consequently, no appreciable SHG is observed for both electron and hole injections ([Figure 2e,f](#)).

Intriguing SHG behavior emerges when we combine both the electric field and charge injection ([Figure 2g–i](#)). In this scenario, the two monolayer K valleys have different energies because of the electric field. When holes are injected into the sample, they reside exclusively in one layer ([Figure 2g](#)). This electronic layer polarization augments their asymmetry, leading to an enhancement of SHG. This can be clearly seen in [Figure 2h,i](#), which displays the SHG map and intensity at varying charge density under a moderate fixed electric field ($E = 0.024$ V/nm). Here E represents the calculated electric field without considering the screening effect of the injected carriers^{22,23} (see the [Supporting Information](#) for the calculation of interlayer electric field with and without considering the free-carrier screening effect).

We can interpret the second-harmonic profile in [Figure 2i](#) across four gating regimes (denoted by the charge density types *n*, *i-i*, *i-p*, and *p-p*) as designated in [Figure 2g,i](#). When the Fermi level resides within the band gap, bilayer WSe_2 is in the *i-i* regime, as both L1 and L2 are intrinsic. Here, the SHG is already observable due to the electric field, just like the SHG in [Figure 2c](#). Upon injecting holes into bilayer WSe_2 , it goes into the *i-p* regime, where L1 remains intrinsic, but L2 becomes populated with holes. Remarkably, the SHG is much enhanced in this regime. In particular, at a hole density of $\sim 4 \times 10^{12}$ cm^{-2} , it becomes five times stronger than in the *i-i* regime. This heightened SHG intensity surpasses the maximum achievable SHG (denoted by a star in [Figure 2c](#)) solely induced by an electric field without charge, limited by the breakdown of gate dielectrics. Therefore, by employing charge injection, we can surpass the dielectric-breakdown limit of field-induced SHG by

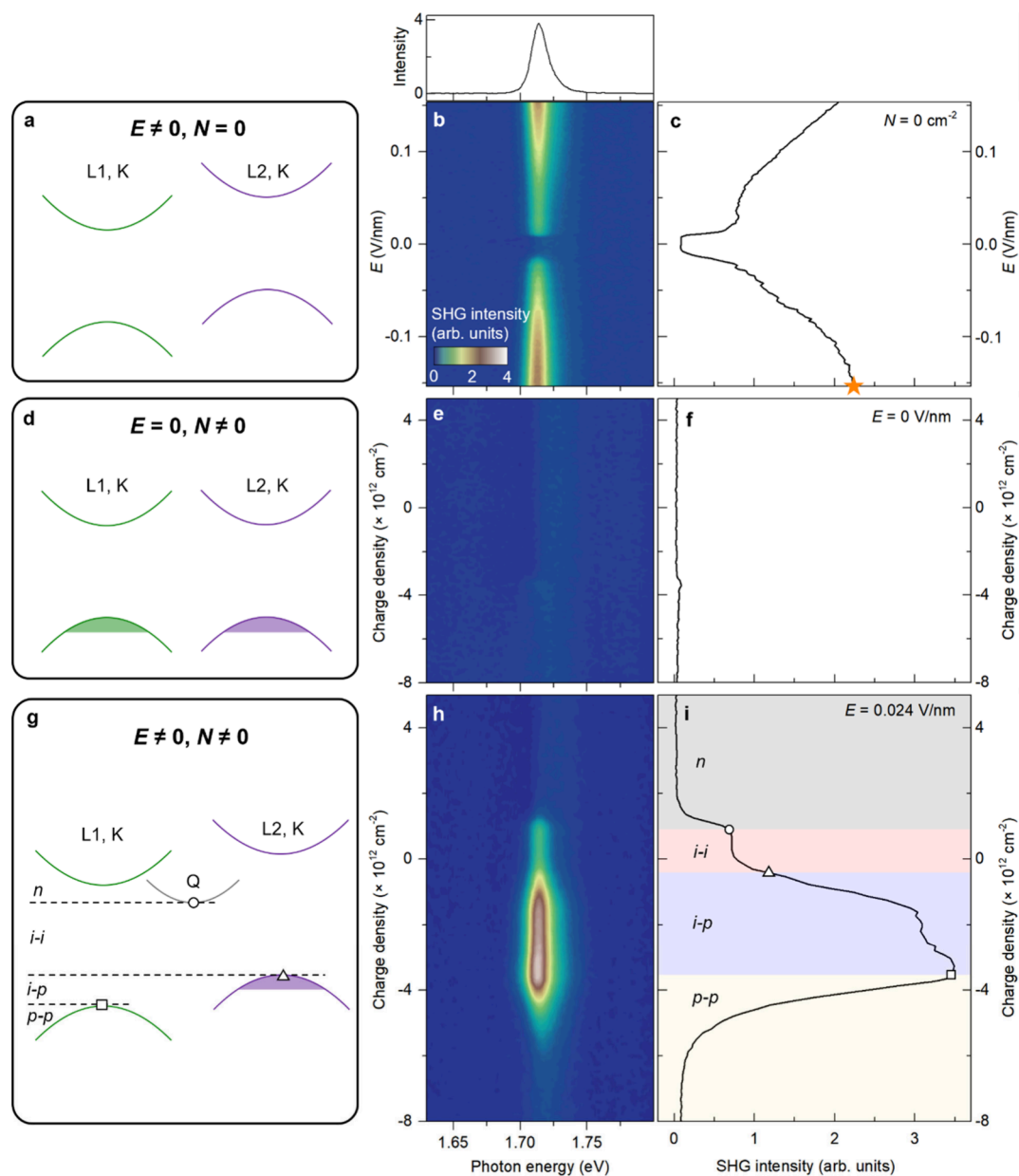


Figure 2. Influences of electric field and charge density on the second-harmonic generation (SHG) of bilayer WSe_2 . (a) Schematic band structure of the K valleys in Layer 1 (L1) and Layer 2 (L2). The application of an out-of-plane electric field E lifts the layer valley degeneracy. (b, c), Second-harmonic spectral map and integrated intensity at varying electric field and zero charge density. Top panel of b displays a representative SHG spectrum. The star at panel c denotes the SHG intensity near dielectric breakdown. (d–f), Similar plots to panels a–c for zero electric field but varying charge density. (g–i) Similar plots for a finite electric field ($E = 0.024$ V/nm) and varying charge density. In panel g, the Q valley is added for clarity. The dashed lines with a circle, triangle, and square denote different critical Fermi levels that define the n , i - i , i - p , and p - p charging regimes of the two layers. These different regimes with corresponding separation symbols are also denoted in panel i.

using an electric field (0.024 V/nm) well below the breakdown critical field (~ 0.15 V/nm).

However, the SHG is quenched when bilayer WSe_2 transitions into the p - p regime, where both L1 and L2 are populated with holes (Figure 2g–i). After the Fermi level reaches the K valley at the other layer (marked by a square in Figure 2g), any additional injected holes are distributed equally between the two layers. These extra holes do not contribute to SHG, but potentially quench it. On the other hand, the SHG is also quenched when we inject electrons to reach the n regime (Figure 2i). This is because the conduction band minimum in bilayer WSe_2 resides in the Q valley (marked by a circle in Figure 2g), not in the K valley. Unlike the layer-localized K-

valley states, the Q-valley states are not confined to one layer. Prior density functional theory (DFT) calculations show that the out-of-plane electric dipole moment of Q-valley electrons is approximately 30% of that of the layer-polarized K-valley holes.²⁰ This delocalized charge distribution of Q-valley electrons persists under an applied electric field. As a result, the accumulated electrons in the Q valleys cannot efficiently break the inversion symmetry to promote SHG. In summary, the SHG is enhanced exclusively in the i - p regime but quenched in the p - p and n regime. Such a sensitive dependence on carrier density and type is uncommon in SHG phenomena.

To explore the mechanism behind the SHG enhancement, we investigated its correlation with excitonic resonances in

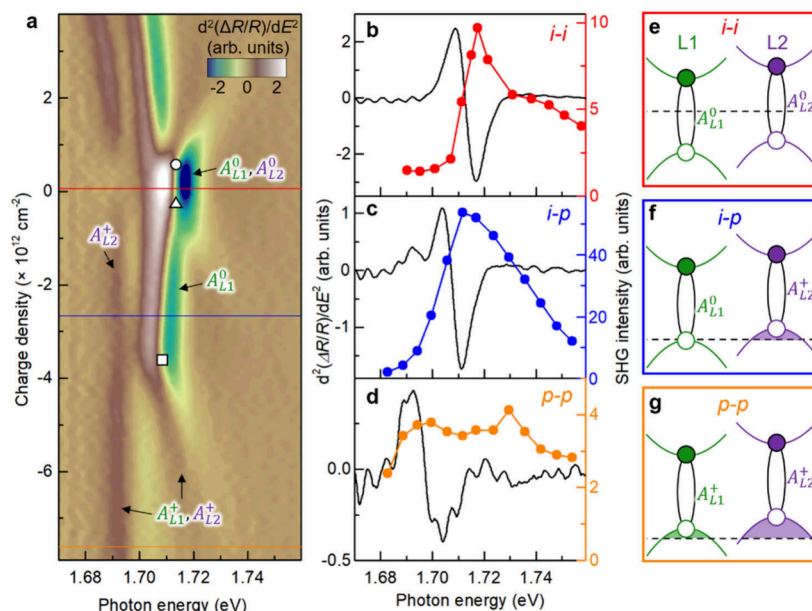


Figure 3. Comparing SHG and excitonic resonances in bilayer WSe₂. (a) Charge-density-dependent color map of the second-order energy derivative of reflectance contrast [$d^2(\Delta R/R)/dE^2$] for bilayer WSe₂ under an out-of-plane electric field $E = 0.024$ V/nm. (b–d) The integrated SHG intensity as a function of double laser photon energy and the $d^2(\Delta R/R)/dE^2$ spectra at three selected charge densities marked by the solid lines with corresponding color in panel a. (e) Band diagram at the red line in panel a. Here both layers (L1, L2) are intrinsic (i - i regime), giving rise to two degenerate intralayer excitons (A_{L1}^0, A_{L2}^0). (f) Band diagram at the blue line in panel a, where L1 is intrinsic but L2 is populated with holes (i - p regime), giving rise to the A_{L1}^0 exciton and A_{L2}^+ intralayer exciton-polaron. (g) Band diagram at the orange line in panel a. Here both layers are populated with holes (p - p regime), giving rise to intralayer exciton-polarons on both layers (A_{L1}^+, A_{L2}^+).

bilayer WSe₂. To this end, we measure the reflectance contrast ($\Delta R/R$) of our bilayer WSe₂ sample and calculate second-order energy derivative $d^2(\Delta R/R)/dE^2$ to reveal subtle features. Figure 3a displays a color map of $d^2(\Delta R/R)/dE^2$ across varying charge densities under a fixed electric field of $E = 0.024$ V/nm. The map shows abrupt changes in excitonic features at critical charge densities (indicated by open symbols), which are attributed to Fermi levels reaching the conduction band minimum (circle), valence band maximum (triangle), and the opposing monolayer's valence band (square), thus defining four distinct regimes: n , i - i , i - p , and p - p (Figures 2g, 3a).

The n regime exhibits optical features from coupled states between K-valley excitons and Q-valley Fermi levels. The i - i regime exhibits an optical feature from two degenerate intralayer excitons (A_{L1}^0, A_{L2}^0) (Figure 3e). Transitioning to the i - p regime reveals two optical features: a strong, higher-energy one attributed to the A_{L1}^0 intralayer exciton and a weak, lower-energy one attributed to the A_{L2}^+ intralayer exciton-polaron^{24–26} (Figure 3a,f). The p - p regime shows two weak optical features, which are attributed to the A_{L1}^+, A_{L2}^+ intralayer exciton-polarons (Figure 3a,g). We neglect the relatively weak interlayer coupling.²⁷

To further explore different gating regimes, we tuned the laser wavelength to sweep the SHG energy across the excitonic spectral range. Figure 3b–d display the $d^2(\Delta R/R)/dE^2$ spectra and the SHG spectra as a function of sweeping two-photon energy in the i - i , i - p , and p - p regimes, respectively. The SHG profiles exhibit two-photon resonant features that correspond closely to excitonic resonances in these regimes.^{11,28,29} Particularly in the i - p regime where SHG peaks exist, a pronounced resonance is observed with the bright A_{L1}^0 state, contrasting with minimal resonance with the dim A_{L2}^+ state (Figure 3a). This distinction suggests that L1 generates strong

second-harmonic signals, while L2 generates weak ones, resulting in a lack of destructive interference between them, as depicted in Figure 1c.

While Figure 3 shows data at a specific electric field ($E = 0.024$ V/nm), systematic adjustment of the electric field modulates the gating regimes. Figure 4a–e present five maps of $d^2(\Delta R/R)/dE^2$ at $E = 0, \pm 0.024$, and ± 0.048 V/nm alongside valley configurations (additional results can be found in the Supporting Information). The n and i - i regimes show minimal variation across electric fields, while the i - p regime expands nearly linearly with increasing field strength because the opposing Stark shifts of L1 and L2 valleys widen their energy separation. In comparison, the field- and density-dependent SHG map (Figure 4f) also shows four distinct regimes, aligning roughly with the n , i - i , i - p , and p - p regimes observed in the reflection measurements (highlighted by lines in Figure 4f). Notably, the SHG is pronounced in the i - p regime, with the density range expanding with an increasing electric field strength.

The comparison of the reflection and SHG data provides crucial insights into the mechanism of SHG enhancement. In the i - i regime, both layers host intralayer exciton states with equal SHG resonant effect, leading to destructive interference and zero net SHG (Figure 1a). Conversely, in the i - p regime, the i -layer with exciton states and the p -layer with exciton-polaron states exhibit distinct resonant behaviors. Prior research showed that exciton polarons have a much weaker resonant effect with SHG than normal excitons.¹¹ When performing SHG at the excitonic resonance, the i -layer emits strong resonant second-harmonic signals, while the p -layer produces weak ones. The lack of destructive interference between them results in pronounced net SHG (Figure 1c). In the p - p regime, both layers host exciton-polaron states with a weak resonant effect, leading to overall weak SHG. Similarly, in

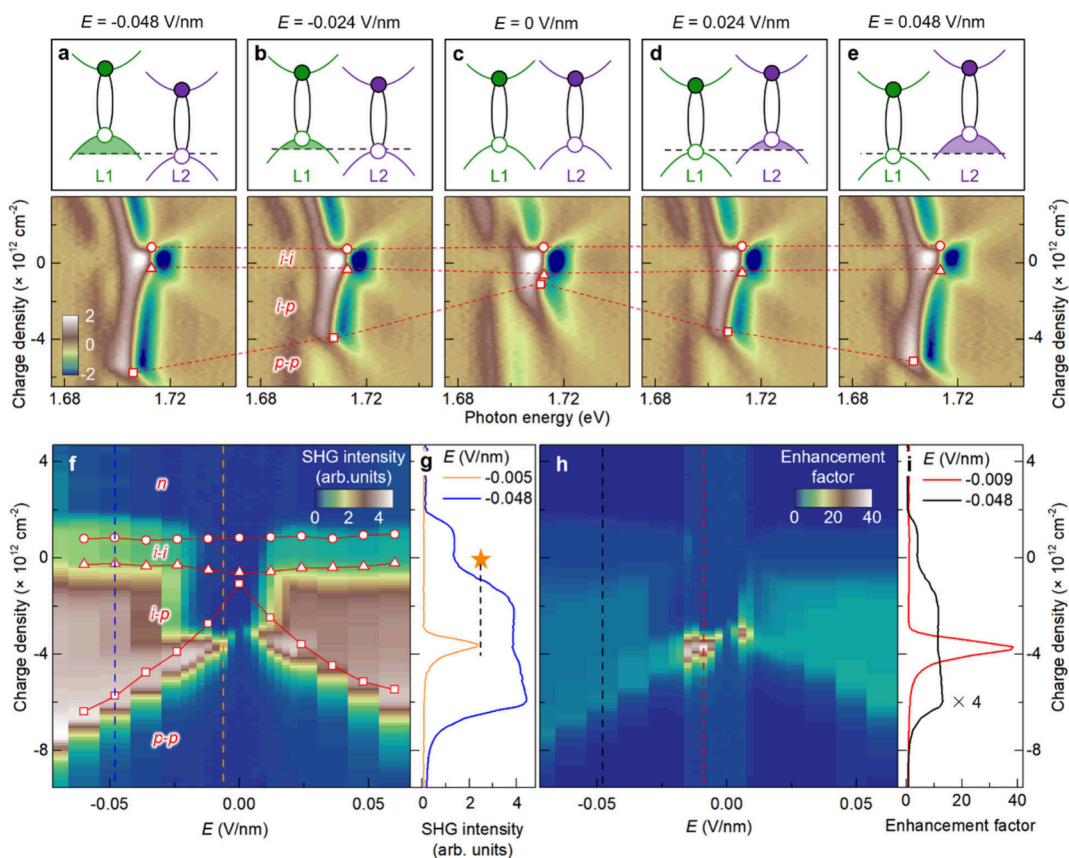


Figure 4. Electric field and charge density modulation of SHG regimes. (a–e) Second-order differential reflectance contrast maps of bilayer WSe_2 along with the corresponding K-valley configurations of the two layers at five different electric fields $E = 0, \pm 0.024$, and ± 0.048 V/nm. Like in Figure 2g, the circles, triangles, and squares denote the critical charge densities where the Fermi level reaches the conduction band, the first valence band, and the second valence valley, respectively. The charge density regions between them define the n , i - i , i - p , and p - p regimes, as delineated by the dashed lines. (f) The SHG intensity color map as a function of charge density and electric field, measured at a laser wavelength of 1449 nm (two-photon energy 1.712 eV). The circles, triangles, and squares mark the critical charge densities obtained from the reflection data, from which the n , i - i , i - p , and p - p regimes are deduced. (g) The charge-density-dependent SHG intensity profile at $E = -0.005$ and -0.048 V/nm. The star denotes the SHG intensity at charge neutrality and $E = -0.15$ V/nm (near dielectric breakdown) as marked in Figure 2c. (h) The SHG enhancement ratio, extracted from panel f, relative to the SHG intensity at zero charge density under the same electric field. (i) Two cross-cut profiles along the red and black dashed lines ($E = -0.009$ and -0.048 V/nm) in panel h. The black profile is magnified by 4 times for clarity.

the n -type regime where the Q-valley electrons distribute across both layers, the exciton polaron states form across both layers, resulting in weak SHG.

We observe a striking phenomenon upon scrutinizing the weak-field region in Figure 4f. Here the field, exemplified by $E = 0.005$ V/nm (indicated by the orange dashed line), accounts for only $\sim 3\%$ of the critical field $E \sim 0.15$ V/nm, as denoted by the star in Figure 2c near the dielectric breakdown. At this field strength, SHG remains negligible in the charge-neutrality regime, indicating that the field strength is insufficient to stimulate SHG. However, within this field range, the SHG experiences a sudden enhancement to a robust intensity within a narrow band of hole density around $3.1 \times 10^{12} \text{ cm}^{-2}$, as depicted by the cross-cut orange profile in Figure 4g. This SHG intensity closely rivals the maximum achievable SHG at $E = 0.15$ V/nm (near the dielectric breakdown) with no charge injection, as marked by the star in Figures 2c and 4h. Essentially, by precisely injecting charges into bilayer WSe_2 , we can achieve highly efficient SHG, comparable to the SHG near the dielectric breakdown with no charge, with a mere $\sim 3\%$ of the breakdown critical field. This underscores an exceptionally sensitive and efficient method for controlling the SHG.

To quantify the enhanced efficiency of SHG, Figure 4h presents a map of the enhancement ratio across various charge densities (y -axis) relative to the SHG intensity at zero charge density under the same electric field (x -axis). Across most of the i - p regime, the enhancement ratio ranges between 3 and 5, as illustrated by the black cross-cut profile in Figure 4i. However, within narrow ranges near a charge density around $4 \times 10^{12} \text{ cm}^{-2}$ and electric fields $E = \pm 0.01$ V/nm, the enhancement ratio peaks at about 40, as indicated by the red cross-cut profile in Figure 4i. This underscores the remarkable efficiency enhancement achieved through our strategy.

In conclusion, we demonstrate an approach to enhance SHG in bilayer WSe_2 by leveraging the strong excitonic resonance and layer-dependent exciton-polaron effect. Our findings also reveal a remarkable sensitivity of SHG to carrier density and carrier type with distinct enhancement and quenching observed in different gating regimes. This detailed understanding paves the way for advanced manipulation of SHG in bilayer WSe_2 and potentially some other 2D materials. Given the intimate relationship between SHG and intralayer excitonic response, SHG holds promise as a sensitive probe for exploring layer-dependent quantum states in 2D materials.^{30,31} Furthermore, our analysis on the critical points of the i - p to p - p

transition suggests that many-body interactions play a crucial role on the electrostatic properties of bilayer WSe₂ (see Section 5 in the Supporting Information).^{32–34} Such interactions may be related to the U-shaped contour observed in the SHG map at low carrier densities (Figure 4f) and the sharp SHG enhancement at low electric fields (Figure 4h), which are not anticipated from the reflectance contrast data (empty symbols in Figure 4f). Further research is merited to explore the potential of using SHG as a sensitive probe for investigating many-body interactions in 2D materials.

METHODS

Device Fabrication. We fabricate dual-gate bilayer WSe₂ devices encapsulated by hexagonal boron nitride on a silicon substrate with a 285 nm SiO₂ epilayer. Initially, we employed standard electron beam lithography and electron beam evaporation techniques to deposit 5 nm-thick titanium/50 nm-thick gold electrodes onto SiO₂/Si substrates. Next, thin graphite flakes, BN flakes, and bilayer WSe₂ flakes are exfoliated from their bulk crystals onto SiO₂/Si substrates. Our bulk WSe₂ crystals are procured from HQ Graphene Incorporation. Subsequently, a dry transfer method is utilized to stack these different thin crystal flakes together. Sequentially, we use polycarbonate stamps to pick up a thin graphite flake (serving as the top-gate electrode), a BN flake (top-gate dielectric), bilayer WSe₂, a second graphite flake (contact electrode), another BN flake (bottom-gate dielectric), and a third graphite flake (bottom-gate electrode). Finally, the stack of materials is transferred onto a prepatterned SiO₂/Si substrate, ensuring proper alignment of the graphite electrodes with the Ti/Au prepatterned electrodes on the substrate.

Reflectance Contrast Measurement. The reflection contrast measurements are conducted using an optical cryostat (Montana Instruments) with an estimated sample temperature of approximately 6 K. A broad-band light source from Thorlabs (SLS201L) is employed for these measurements. The white light is focused onto the sample by a microscope objective with a numerical aperture of 0.6, resulting in a spot diameter of ~2 μm on the sample surface. Subsequently, the reflected light is collected by the same objective and directed toward a high-resolution spectrometer (Princeton Instruments) equipped with a charge-coupled-device (CCD) camera (Princeton Instruments, PIXIS 400) for analysis. To obtain a reflectance contrast spectrum of bilayer WSe₂, two spectra are measured: one from the sample area containing bilayer WSe₂ (referred to as R_s) and another from a nearby reference area lacking bilayer WSe₂ (referred to as R_r, specifically the Gr/BN/BN/Gr area). The reflectance contrast is calculated using the formula $\Delta R/R = (R_s - R_r)/R_r$. To enhance the visibility of weak features, we computed the second-order energy derivative of the $\Delta R/R$ spectra.

Second-Harmonic-Generation Measurement. In our SHG experiment, we utilized an ultrafast laser system (PHAROS + ORPHEUS) provided by Light Conversion. The light source comes from a mode-locked Yb:KGW laser (PHAROS) with a control emission wavelength of 1030 nm and a repetition rate of 250 kHz. Through an optical parametric amplifier (ORPHEUS), the laser wavelength is converted to the infrared range (1400–1500 nm). The infrared beam is focused onto the sample using a microscope objective (NA = 0.6). The spot diameter is ~2 μm on the sample. The generated second-harmonic signal is collected by the same objective, then filtered through an 800 nm short-pass filter

(Thorlabs, FESH0800) to block the excitation beam. Subsequently, the signal is analyzed by a high-resolution spectrometer (Princeton Instruments) equipped with a CCD camera (Princeton Instruments, PIXIS 400). Linear polarizers and half-wave plates are inserted into the beam path to control the polarization of the excitation laser and measure the polarization of the detected light.

ASSOCIATED CONTENT

Supporting Information

The Supporting Information is available free of charge at <https://pubs.acs.org/doi/10.1021/acs.nanolett.4c04544>.

Details on the device characterization, power and polarization dependence of SHG, reflection contrast measurements, calculation of the interlayer electric field, analysis of the *i-p* to *p-p* transition point, and SHG measurement on Device 2 (PDF)

AUTHOR INFORMATION

Corresponding Authors

Nathaniel M. Gabor – Department of Physics and Astronomy, University of California Riverside, Riverside, California 92521, United States; orcid.org/0000-0002-0351-2787; Email: nathaniel.gabor@ucr.edu

Chun Hung Lui – Department of Physics and Astronomy, University of California Riverside, Riverside, California 92521, United States; Email: joshua.lui@ucr.edu

Authors

Soonyoung Cha – Department of Physics and Astronomy, University of California Riverside, Riverside, California 92521, United States; orcid.org/0009-0009-9973-0372

Tianyi Ouyang – Department of Physics and Astronomy, University of California Riverside, Riverside, California 92521, United States

Takashi Taniguchi – International Center for Materials Nanoarchitectonics, National Institute for Materials Science, Tsukuba 305-0044, Japan; orcid.org/0000-0002-1467-3105

Kenji Watanabe – Research Center for Functional Materials, National Institute for Materials Science, Tsukuba 305-0044, Japan; orcid.org/0000-0003-3701-8119

Complete contact information is available at: <https://pubs.acs.org/10.1021/acs.nanolett.4c04544>

Author Contributions

S.C. and T.O. contributed equally.

Notes

The authors declare no competing financial interest.

ACKNOWLEDGMENTS

C.H.L. acknowledges support from the National Science Foundation (NSF) Division of Materials Research CAREER Award No. 1945660 and from the American Chemical Society Petroleum Research Fund No. 61640-ND6. K.W. and T.T. acknowledge support from the JSPS KAKENHI (Grant Numbers 19H05790, 20H00354, and 21H05233). N.M.G. and S.C. were supported by ARO MURI grant no. W911NK-24-1-0292 and the Army Research Office Electronics Division Award no. W911NF2110260. N. M. G. was also supported by the Presidential Early Career Award for Scientists and

Engineers (PECASE) through the Air Force Office of Scientific Research (award no. FA9550-20-1-0097).

REFERENCES

- (1) Shen, Y. R. *The Principles of Nonlinear Optics*; Wiley, 1984.
- (2) Lee, C. H.; Chang, R. K.; Bloembergen, N. Nonlinear electroreflectance in silicon and silver. *Phys. Rev. Lett.* **1967**, *18* (5), 167–170.
- (3) Terhune, R. W.; Maker, P. D.; Savage, C. M. Optical harmonic generation in calcite. *Phys. Rev. Lett.* **1962**, *8* (10), 404–406.
- (4) Li, Y.; Rao, Y.; Mak, K. F.; You, Y.; Wang, S.; Dean, C. R.; Heinz, T. F. Probing symmetry properties of few-layer MoS₂ and h-BN by optical second-harmonic generation. *Nano Lett.* **2013**, *13* (7), 3329–3333.
- (5) Säynätjoki, A.; Karvonen, L.; Rostami, H.; Autere, A.; Mehravar, S.; Lombardo, A.; Norwood, R. A.; Hasan, T.; Peyghambarian, N.; Lipsanen, H.; Kieu, K.; Ferrari, A. C.; Polini, M.; Sun, Z. Ultra-strong nonlinear optical processes and trigonal warping in MoS₂ layers. *Nat. Commun.* **2017**, *8* (1), 893.
- (6) Hsu, W.-T.; Zhao, Z.-A.; Li, L.-J.; Chen, C.-H.; Chiu, M.-H.; Chang, P.-S.; Chou, Y.-C.; Chang, W.-H. Second harmonic generation from artificially stacked transition metal dichalcogenide twisted bilayers. *ACS Nano* **2014**, *8* (3), 2951–2958.
- (7) Shan, Y.; Li, Y.; Huang, D.; Tong, Q.; Yao, W.; Liu, W.-T.; Wu, S. Stacking symmetry governed second harmonic generation in graphene trilayers. *Sci. Adv.* **2018**, *4* (6), No. eaat0074.
- (8) Yao, K.; Finney, N. R.; Zhang, J.; Moore, S. L.; Xian, L.; Tancogne-Dejean, N.; Liu, F.; Ardelean, J.; Xu, X.; Halbertal, D.; Watanabe, K.; Taniguchi, T.; Ochoa, H.; Asenjo-Garcia, A.; Zhu, X.; Basov, D. N.; Rubio, A.; Dean, C. R.; Hone, J.; Schuck, P. J. Enhanced tunable second harmonic generation from twistable interfaces and vertical superlattices in boron nitride homostructures. *Sci. Adv.* **2021**, *7* (10), No. eabe8691.
- (9) Fan, X.; Jiang, Y.; Zhuang, X.; Liu, H.; Xu, T.; Zheng, W.; Fan, P.; Li, H.; Wu, X.; Zhu, X.; Zhang, Q.; Zhou, H.; Hu, W.; et al. Broken symmetry induced strong nonlinear optical effects in spiral WS₂ nanosheets. *ACS Nano* **2017**, *11* (5), 4892–4898.
- (10) Malard, L. M.; Alencar, T. V.; Barboza, A. P. M.; Mak, K. F.; de Paula, A. M. Observation of intense second harmonic generation from MoS₂ atomic crystals. *Phys. Rev. B* **2013**, *87* (20), 201401R.
- (11) Seyler, K. L.; Schaibley, J. R.; Gong, P.; Rivera, P.; Jones, A. M.; Wu, S.; Yan, J.; Mandrus, D. G.; Yao, W.; Xu, X. Electrical control of second-harmonic generation in a WSe₂ monolayer transistor. *Nat. Nanotechnol.* **2015**, *10* (5), 407–411.
- (12) Zhang, M.; Han, N.; Wang, J.; Zhang, Z.; Liu, K.; Sun, Z.; Zhao, J.; Gan, X. Strong second harmonic generation from bilayer graphene with symmetry breaking by redox-governed charge doping. *Nano Lett.* **2022**, *22* (11), 4287–4293.
- (13) Mennel, L.; Furchi, M. M.; Wächter, S.; Paur, M.; Polyushkin, D. K.; Mueller, T. Optical imaging of strain in two-dimensional crystals. *Nat. Commun.* **2018**, *9* (1), 516.
- (14) Zhang, M.; Han, N.; Zhang, J.; Wang, J.; Chen, X.; Zhao, J.; Gan, X. Emergent second-harmonic generation in van der Waals heterostructure of bilayer MoS₂ and monolayer graphene. *Sci. Adv.* **2023**, *9* (11), No. eadf4571.
- (15) Wang, Y.; Xiao, J.; Chung, T.-F.; Nie, Z.; Yang, S.; Zhang, X. Direct electrical modulation of second-order optical susceptibility via phase transitions. *Nat. Electron.* **2021**, *4*, 725–730.
- (16) Lin, K.-Q.; Bange, S.; Lupton, J. M. Quantum interference in second-harmonic generation from monolayer WSe₂. *Nat. Phys.* **2019**, *15* (3), 242–246.
- (17) Yu, H.; Talukdar, D.; Xu, W.; Khurgin, J. B.; Xiong, Q. Charge-induced second-harmonic generation in bilayer WSe₂. *Nano Lett.* **2015**, *15* (8), 5653–5657.
- (18) Klein, J.; Wierzbowski, J.; Steinhoff, A.; Florian, M.; Rösner, M.; Heimbach, F.; Müller, K.; Jahnke, F.; Wehling, T. O.; Finley, J. J.; Kaniber, M. Electric-field switchable second-harmonic generation in bilayer MoS₂ by inversion symmetry breaking. *Nano Lett.* **2017**, *17* (1), 392–398.
- (19) Wang, J.; Han, N.; Luo, Z.-D.; Zhang, M.; Chen, X.; Liu, Y.; Hao, Y.; Zhao, J.; Gan, X. Electrically tunable second harmonic generation in atomically thin ReS₂. *ACS Nano* **2022**, *16* (4), 6404–6413.
- (20) Altaïry, M. M.; Liu, E.; Liang, C.-T.; Hsiao, F.-C.; van Baren, J.; Taniguchi, T.; Watanabe, K.; Gabor, N. M.; Chang, Y.-C.; Lui, C. H. Electrically switchable intervalley excitons with strong two-phonon scattering in bilayer WSe₂. *Nano Lett.* **2022**, *22* (5), 1829–1835.
- (21) Kunstmann, J.; Mooshammer, F.; Nagler, P.; Chaves, A.; Stein, F.; Paradiso, N.; Plechinger, G.; Strunk, C.; Schüller, C.; Seifert, G.; Reichman, D. R.; Korn, T. Momentum-space indirect interlayer excitons in transition-metal dichalcogenide van der Waals heterostructures. *Nat. Phys.* **2018**, *14* (8), 801–805.
- (22) Wang, Z.; Chiu, Y.-H.; Honz, K.; Mak, K. F.; Shan, J. Electrical tuning of interlayer exciton gases in WSe₂ bilayers. *Nano Lett.* **2018**, *18* (1), 137–143.
- (23) Lin, K.-Q.; Faria Junior, P. E.; Hübner, R.; Ziegler, J. D.; Bauer, J. M.; Buchner, F.; Florian, M.; Hofmann, F.; Watanabe, K.; Taniguchi, T.; Fabian, J.; Steinhoff, A.; Chernikov, A.; Bange, S.; Lupton, J. M. Ultraviolet interlayer excitons in bilayer WSe₂. *Nat. Nanotechnol.* **2024**, *19* (2), 196–201.
- (24) Mak, K. F.; He, K.; Lee, C.; Lee, G. H.; Hone, J.; Heinz, T. F.; Shan, J. Tightly bound trions in monolayer MoS₂. *Nat. Mater.* **2013**, *12* (3), 207–211.
- (25) Efimkin, D. K.; MacDonald, A. H. Many-body theory of trion absorption features in two-dimensional semiconductors. *Phys. Rev. B* **2017**, *95* (3), No. 035417.
- (26) Liu, E.; van Baren, J.; Lu, Z.; Taniguchi, T.; Watanabe, K.; Smirnov, D.; Chang, Y.-C.; Lui, C. H. Exciton-polaron Rydberg states in monolayer MoSe₂ and WSe₂. *Nat. Commun.* **2021**, *12* (1), 6131.
- (27) Pisoni, R.; Davatz, T.; Watanabe, K.; Taniguchi, T.; Ihn, T.; Ensslin, K. Absence of interlayer tunnel coupling of K-valley electrons in bilayer MoS₂. *Phys. Rev. Lett.* **2019**, *123* (11), 117702.
- (28) Yin, X.; Ye, Z.; Chenet, D. A.; Ye, Y.; O'Brien, K.; Hone, J. C.; Zhang, X. Edge nonlinear optics on a MoS₂ atomic monolayer. *Science* **2014**, *344* (6183), 488–490.
- (29) Wang, G.; Marie, X.; Gerber, I.; Amand, T.; Lagarde, D.; Bouet, L.; Vidal, M.; Balocchi, A.; Urbaszek, B. Giant enhancement of the optical second-harmonic emission of WSe₂ monolayers by laser excitation at exciton resonances. *Phys. Rev. Lett.* **2015**, *114* (9), No. 097403.
- (30) Xu, X.; Yao, W.; Xiao, D.; Heinz, T. F. Spin and pseudospins in layered transition metal dichalcogenides. *Nat. Phys.* **2014**, *10* (5), 343–350.
- (31) Shi, Q.; Shih, E.-M.; Rhodes, D.; Kim, B.; Barmak, K.; Watanabe, K.; Taniguchi, T.; Papić, Z.; Abanin, D. A.; Hone, J.; Dean, C. R. Bilayer WSe₂ as a natural platform for interlayer exciton condensates in the strong coupling limit. *Nat. Nanotechnol.* **2022**, *17* (6), 577–582.
- (32) Riley, J. M.; Meevasana, W.; Bawden, L.; Asakawa, M.; Takayama, T.; Eknapakul, T.; Kim, T. K.; Hoesch, M.; Mo, S.-K.; Takagi, H.; Sasagawa, T.; Bahramy, M. S.; King, P. D. C. Negative electronic compressibility and tunable spin splitting in WSe₂. *Nat. Nanotechnol.* **2015**, *10* (12), 1043–1047.
- (33) Xu, Y.; Kang, K.; Watanabe, K.; Taniguchi, T.; Mak, K. F.; Shan, J. A tunable bilayer Hubbard model in twisted WSe₂. *Nat. Nanotechnol.* **2022**, *17* (9), 934–939.
- (34) Skinner, B.; Shklovskii, B. I. Anomalously large capacitance of a plane capacitor with a two-dimensional electron gas. *Phys. Rev. B* **2010**, *82* (15), 155111.